Article

Deconstructing Electrostatics of Functionalized Metal Nanoparticles from Molecular Dynamics Simulations

Margherita Bini, Valentina Tozzini,* and Giorgia Brancolini*

Cite This: *J. Phys. Chem. B* 2023, 127, 8226−8241
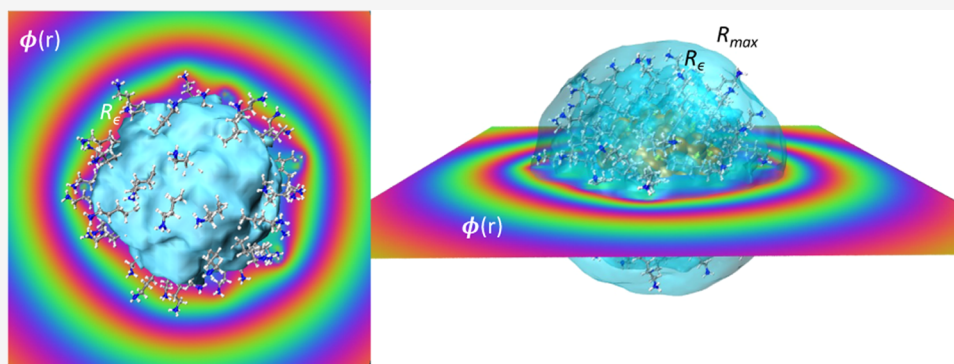
Read Online

ACCESS | Metrics & More | Article Recommendations | Supporting Information

ABSTRACT: Gold nanoparticles (NPs) with different surface functionalizations can selectively interact with specific proteins, allowing a wide range of possible applications in biotechnology and biomedicine. To prevent their tendency to aggregate and to modulate their interaction with charged biomolecules or substrates (e.g., for biosensing applications), they can be functionalized with charged groups, introducing a mutual interaction which can be modulated by changing the ionic strength of the solvent. *In silico* modeling of these systems is often addressed with low-resolution models, which must account for these effects in the, often implicit, solvent representation. Here, we present a systematic conformational dynamic characterization of ligand-coated gold nanoparticles with different sizes, charges, and functionalizations by means of atomistic molecular dynamics simulations. Based on these, we deconstruct their electrostatic properties and propose a general representation of their average-long-range interactions extendable to different sizes, charges, and ionic strengths. This study clarifies in detail the role of the different features of the NP (charge, size, structure) and of the ionic strength in determining the details of the interparticle interaction and represents the first step toward a general strategy for the parametrization of NP coarse-grained models able to account for varying ionic strengths.

INTRODUCTION

In the last few years, there has been a growing interest in gold nanoparticles (NPs)[1] with surfaces functionalized with a variety of ligands[2] proposed for a wide range of applications[3,4] in biotechnology and biomedicine,[5] such as biosensing and theranostics.[6,7] However, NP use requires deep control of their chemical-physical properties. For instance, their function is often limited by their tendency to aggregate due to hydrophobic surfaces. Functionalization with charged ligands can help stabilize NP suspensions, further endowing them with interesting properties for the biosensing of charged biological substrates.[8,9]

The optimization of the size, charge, and functionalization of the NPs for specific applications can greatly benefit computer modeling.[10] Recently, atomistic molecular dynamics (MD) simulations of gold NPs (AuNPs) covalently functionalized with charged groups[11,12] have highlighted the role played by solvents and counterions, which form intimately assembled complexes with the NPs and mediate their interactions. Ionic-strength-dependent electrostatics was also confirmed as the main determinant of complexation of AuNPs with nanomaterials and biological molecules.[9,13−15] Atomistic models provide an invaluable amount of information not accessible to experiment, but the optimization of the NP size and functionalization requires the extensive *in silico* exploration of a huge parameter space, varying the intrinsic NP features and the environmental conditions. The need for computationally cheaper simulations has therefore triggered considerable efforts to build low-resolution models for biofunctionalized NPs.[16−20] "Double scale" representations with a large bead for the gold core decorated with smaller beads for the ligands[21,22] have the advantage of matching with the residue-based models for
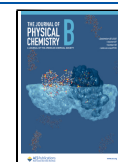
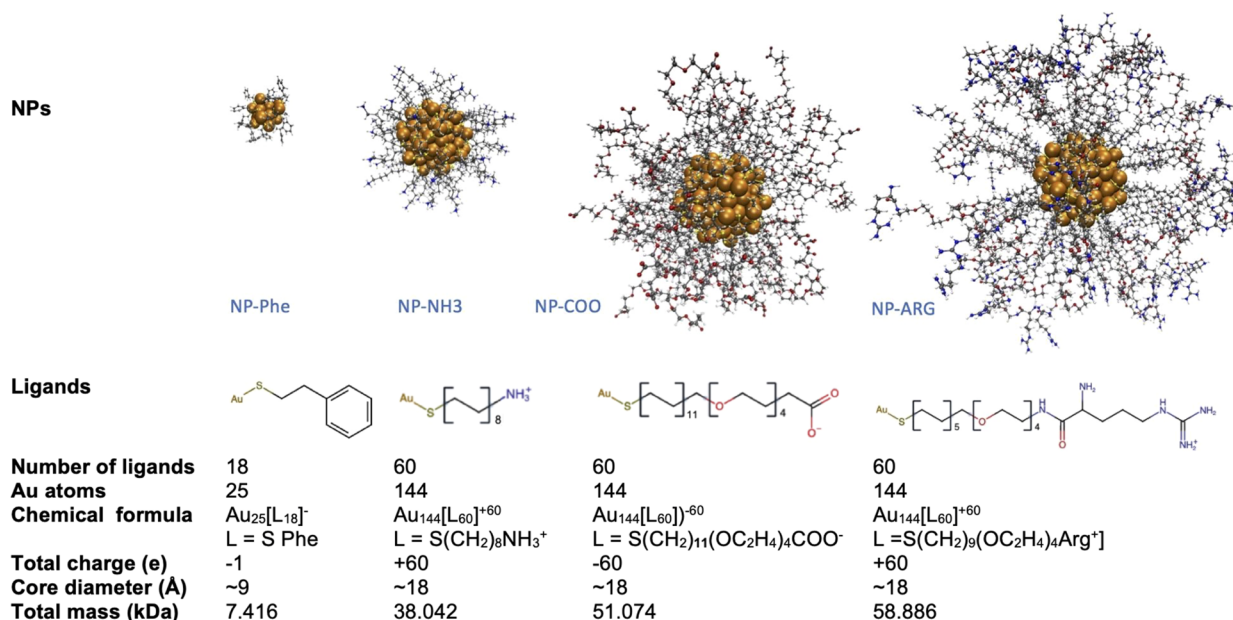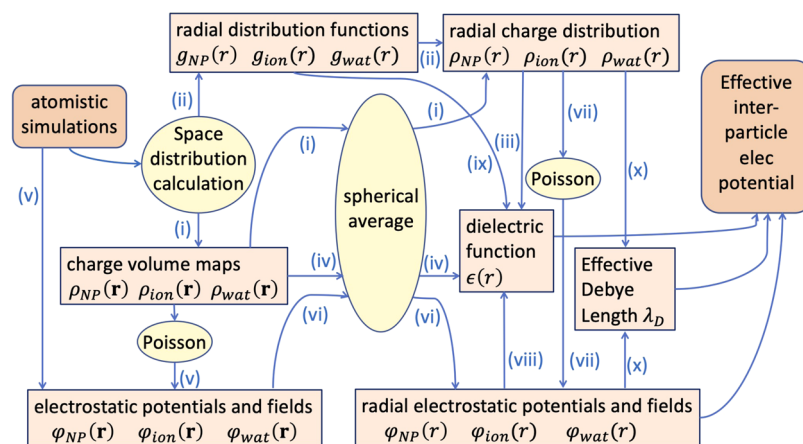**Scheme 1. Flowchart of Electrostatic Analysis and Calculations**

Figure 1. Model systems considered in this work (names aside from the structures). Color coding of the structures: orange, Au; Ligands: C, black; O, red; N, blue; H, white; S, yellow. Same color coding in the chemical sketches of the ligands, reported under the structures. Values of other parameters are reported in subsequent rows for each NP, as indicated.

proteins,[23,24] to simulate mixtures. On the other hand, coarser models treating the NP as a single spherical object[25,26] are cheaper and ideal for extensive *in silico* exploration. In all cases, the presence of a net charge and the use of an implicit solvent make it compulsory the use of advanced electrostatic treatments.[27]

We recently started the systematic building of biofunctionalized NP models using simple guiding principles:[28] minimum computational cost, compatibility with available low-resolution models for proteins, capability of working in different environmental conditions, and extendability to different sizes and functionalizations. In other works, we apply these principles to the Double scale model, especially focusing on the compatibility and extendability problems.[29,30] Here, we focus on the accurate parametrization of the electrostatics and its dependence on ionic strength, being relevant, e.g., for biosensing due to dielectric screening at physiological ionic strengths. To this aim, we combine data from atomistic simulations with the Debye−Hückel (DH)-like potential within a mixed bottom-up−top-down strategy.[31,32]

This work is organized as follows. After the detailed description of simulations and electrostatic analysis methodology, we first analyze the atomistic simulations of a number of exemplar NPs of different sides and charges and at different ionic strengths and determine the space distributions of side chains and charges. From these, we derive the electrostatic potentials, which are then used to fit the DH parameters,[33] including the renormalization of NP charges and radii. The derived analytic potential includes the electrostatic contribution of both surface chemistry elements and solvent/ions mimicking the effect of different ionic strengths.

■ METHODS AND THEORETICAL FRAMEWORK

The flowchart of electrostatic calculations is reported in Scheme 1. Starting from the atomistic simulations, the space distributions of the atoms of the NPs, of water, and of ions are evaluated separately to obtain the charge spatial distribution functions $\rho(\mathbf{r})$ evaluated on grids around the particles and their spherical averages $\rho(r)$. From these, the electrostatic potentials,

Table 1. List of Simulations[a]

		sim box (nm^3)	ions	λ_D (nm)	IOS (mM)
1	NP-Phe	7.5 × 7.5 × 7.5	1 Na$^+$	6.92	2 (0)
2	NP-NH3	6.255 × 6.228 × 6.241	60 Cl$^-$	0.67 (∞)	218 (0)
3	NP-NH3	12.00 × 12.00 × 12.00	51 Na$^+$, 111 Cl$^-$	1.10 (1.38)	79 (50)
4	NP-NH3	12.00 × 12.00 × 12.00	154 Na$^+$, 214 Cl$^-$	0.73 (0.79)	119 (100)
5	NP-NH3	12.00 × 12.00 × 12.00	361 Na$^+$, 421 Cl$^-$	0.50 (0.52)	216 (200)
6	NP-COO	19.00 × 12.00 × 12.00		∞	0
7	NP-COO	18.00 × 12.00 × 12.00	60 Na$^+$	2.28 (∞)	19 (0)
8	NP-COO	18.00 × 12.00 × 12.00	138 Na$^+$, 78 Cl$^-$	1.20 (1.41)	69 (50)
9	NP-COO	18.00 × 12.00 × 12.00	216 Na$^+$, 156 Cl$^-$	0.89 (0.97)	119 (100)
10	NP-COO	18.00 × 12.00 × 12.00	372 Na$^+$, 312 Cl$^-$	0.66 (0.69)	219 (200)
11	NP-Arg	19.00 × 12.00 × 12.00		∞	0
12	NP-Arg	18.08 × 12.06 × 12.06	60 Cl$^-$	2.23 (∞)	19 (0)
13	NP-Arg	18.08 × 12.06 × 12.06	79 N$^+$, 139 Cl$^-$	1.20 (1.40)	68 (50)
14	NP-Arg	18.08 × 12.06 × 12.06	158 Na$^+$, 218 Cl$^-$	0.89 (0.97)	118 (100)
15	NP-Arg	18.08 × 12.06 × 12.06	317 Na$^+$, 377 Cl$^-$	0.66 (0.69)	218 (200)

[a]Equilibration run length: 100 ps. Production run: 200 ns (except for number 1, 250 ns). Debye length $\lambda_D^2 = 1/(4\pi\lambda_B(n_+ + n_-))$ nm^2; $n\pm$ = ionic densities and λ_B Bjerrum length in water at RT $\sim$ 0.7 nm. The ionic strengths, IOS, $I = 1/2(n_+ + n_-)$, are reported both considering all of the ions or only those in excess of the neutralizing ones (in ()).

the dielectric function $\epsilon(r)$, and the Debye lengths λ_D are evaluated and, subsequently, the inter-NP potential. Details are reported in the following subsections.

Model Systems and Simulation Setup. The NPs considered in this work are reported in Figure 1: a small one with a gold core of 25 Au atoms, functionalized with 18 phenylalanine-like groups and with −1 charge (NP-Phe), and three with a larger (Au144) gold core, with 60 ligands consisting of short PE (polyethylene) + PEG [poly(ethylene glycol)] chains terminated with an ammonium group, a carboxylic group, or an arginine, named NP-NH3, NP-COO, and NP-Arg, respectively. The covalent linkage between the functional groups and the core occurs through a S atom bridging two Au atoms. The shape of the gold depends on the number of Au atoms and on the number and chemical nature of the ligands. The atoms of the core are arranged in shells, differing for the two types of cores: Au25 has one Au atom in the center surrounded by 12 gold atoms arranged in two shells with an icosahedral symmetry; conversely, Au144 has more layers with icosahedral centers and a more globular overall shape.[34] The symmetry of ligand location on the surface and the geometry of the S-bridge depend on the symmetry of the core, making NP-Phe different from the others in these respects. Details on this aspect are reported in the Supporting Information (SI) (Section S.1).

The performed MD simulations are listed in Table 1. For the NP-Arg, NP-COO, and NP-NH3, different ionic strengths were considered (number of counterions reported). Using a previously established protocol,[35] we generated NP topologies with the TPPmktop server[36] and fully hydrated the systems in simulation boxes of up to ~2 nm side. We developed the parameters for Au[37] in line with the GolP FF for nanoclusters[38] and used the OPLS/AA force field for the ligands and the SPC/E for water. RESP (restrained electrostatic potential) charges[14,35,39] were generated using the RED server[40] (further details in the SI, Section S.3). MD equations were integrated with the leapfrog algorithm (with Δt = 2 or 1 fs) keeping frozen the gold core and restraining the bond lengths with LINCS5[41] (tolerance: 0.0001). During the production phase, NPT-room temperature conditions were maintained by means of the Bussi−Donadio−Parrinello

thermostat[42] and the Parrinello−Raman barostat.[43] The interaction cutoff was set at 1.1 nm, using the particle-mesh Ewald summation scheme[44] for electrostatics. Simulations were performed with GROMACS vs5.1.5,[45] while in-house coded scripts were used to automate the data production and the input parameter generation. Table 1 also reports the ionic strengths and corresponding λ_D's evaluated by using either all of the ions in solution or only those in excess with respect to the neutralizing ones.

Space and Radial Distribution Functions. Using the trajectories with gold cores aligned, the charge distributions for NP atoms, water, and ions are evaluated according to Scheme 1. In route (i), the charge volume map is evaluated on a 1 Å resolution grid using the volmap tool of VMD1.9.3,[46] using the effective atomic charges (with a Gaussian smearing using the vdW radius) and averaging over the trajectory frames. Three charge maps $\rho_{NP}(\mathbf{r})$, $\rho_{ion}(\mathbf{r})$, and $\rho_{wat}(\mathbf{r})$ for NPs, ions, and water are calculated and subsequently spherically averaged using in-house-coded Python scripts[47] to obtain the corresponding radial functions $\rho_{NP}(r)$, $\rho_{ion}(r)$, and $\rho_{wat}(r)$. In the alternative route (ii), the $\rho(r)$'s are evaluated from the charge weighted radial distribution functions, namely, with $\rho(r) = \sum_i \frac{N_i}{V} q_i g_i(r) = \sum_i n_i(r) q_i$, where $g_i(r)$ is the pair distribution function between the NP center[a] and the atoms of type i, and N_i, q_i, and $n_i(r)$ are their number, charge, and radial density, respectively. Comparing (i) and (ii) (SI, Section S.2) reveals negligible numerical differences. While (ii) is faster, (i) bears the volumetric information as an intermediate.

The $g(r)$ and $\rho(r)$ are also used to evaluate the particle size. Besides the gyration radius $R_g = \langle R_g(t) \rangle = \langle \sqrt{\sum_{i=1}^{N} m_i |\mathbf{r}_i - \mathbf{R}_{COM}|^2 / \sum_{i=1}^{N} m_i} \rangle$ (with $\mathbf{R}_{COM}$ the location of the NP COM), we define R_{max} as the maximum value of the distance of the apical group center of mass (COM) from the center, and R_{av} is its average value over the production runs.

Dielectric Function. Usually the dielectric function accounting for the implicit solvent polarization screening is assumed to be constant and equal to ϵ_∞ (80 for water) "outside" and $\epsilon_0 = 1$ "inside" a particle. Here, we assume a soft passage across the NP boundary described by a switch function
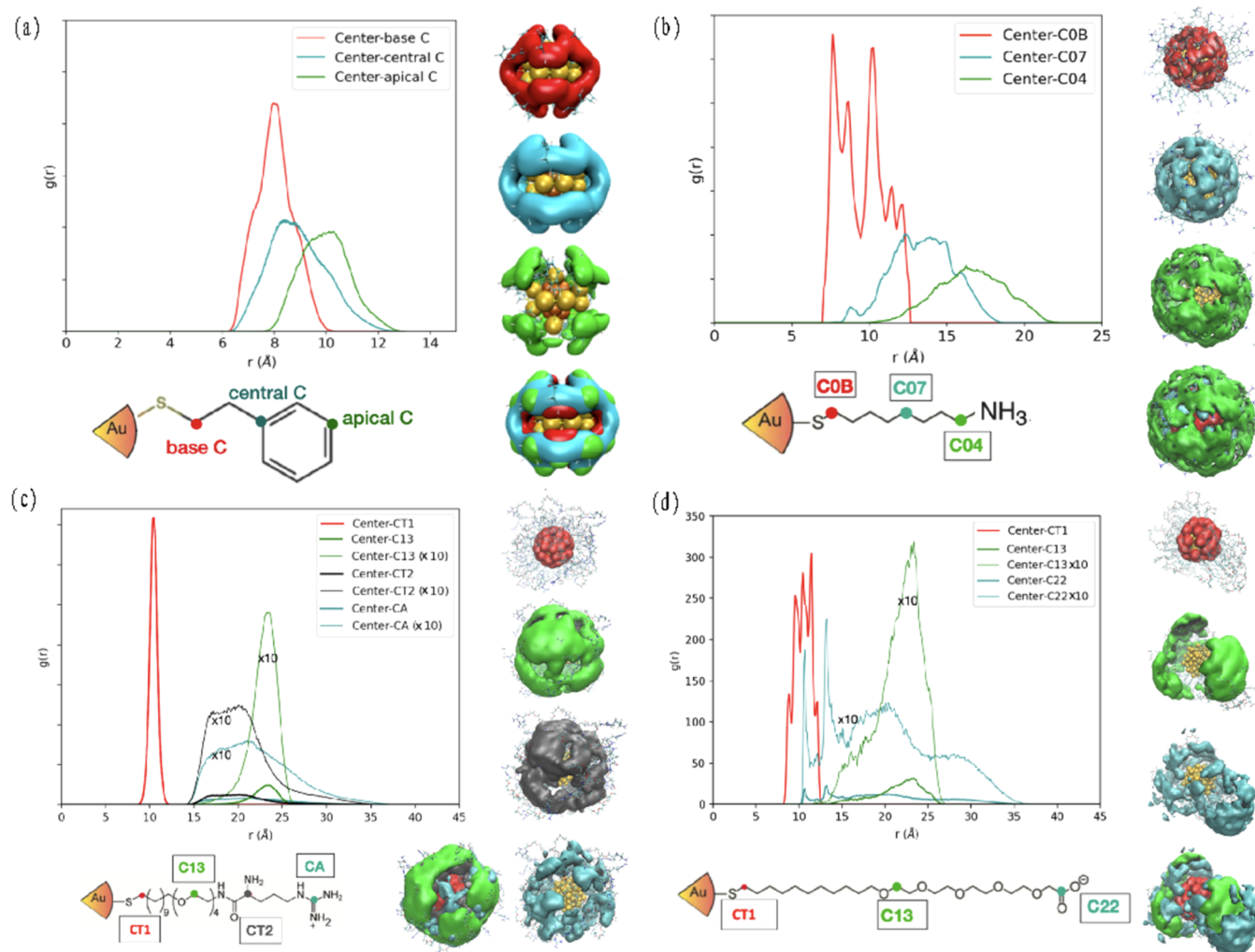
Figure 2. Radial and space distribution functions of selected atom types (indicated) of (a) NP-Phe, (b) NP-NH3, (c) NP-COO, and (d) NP-Arg at small ionic strengths (simulations 1, 2, 7, and 12). The structures aside report the space density distributions of the same atoms as the iso-density surfaces. Selected atoms' colors in the schemes, isosurfaces, and line colors are corresponding. Surfaces are reported separated and superimposed in the last representation and also superimposed to atomistic structures of the NP for reference (Au core atoms in yellow).

$$\epsilon(r) = f_{sw}(R, \sigma, r) = \frac{\epsilon_0 + \epsilon_\infty e^{r - R_c/\sigma}}{1 + e^{r - R_c/\sigma}} \quad (1)$$

depending on a switching of the radius and width, R_c and σ. This definition exploits the space locality of the electric response,[48] often used in biosystems,[49] allowing one to evaluate the full dielectric response from atomistic simulations from the space distribution of the solvent or solute.[50] Assuming that the (r) profile follows that of the water penetration into the NP as described by $\rho_{wat}(r)$, we fit function (eq 1) on it (route (iii)). Alternatively (route (iv)), we use the APBS software[51] to calculate the water penetration by means of the solvent-accessible surface area (SASA) on single representative frames chosen as the largest cluster centroids of each production trajectory. The obtained $\epsilon(\mathbf{r})$ is eventually spherically averaged to obtain $\epsilon(r)$. Route (iv) is less statistically representative than route (iii) but retains the full volumetric information. More details on these aspects can be found in the SI, Section S.4.

Electrostatic Fields and Potentials. The direct calculation of the electrostatic potential route (v)

$$\phi(\mathbf{r}) = \left\langle \sum_i \frac{q_i}{|\mathbf{r} - \mathbf{r_i}|} \right\rangle \quad (2)$$

is carried out by `volmap` with the multilevel summation method (MSM)[52] averaging over the trajectory, for all components separately. Conversely, the Poisson equation (PE, route vi)

$$-\nabla\epsilon(\mathbf{r})\nabla\phi(\mathbf{r}) = 4\pi\rho(\mathbf{r}) \quad (3)$$

is solved for comparison on the representative frames with APBS, setting the boundary ϕ to the Debye–Hückel value at the given ion densities[b]. In both cases, ϕ is returned on a grid and can be spherically averaged to obtain $\phi(r)$. This can be compared to the $\phi(r)$ obtained under the assumption of complete isotropy from the radial $\rho(r)$ (route vii)

$$\rho_{tot}(r) = \rho_{NP}(r) + \rho_{ion}(r) + \rho_{wat}(r) = \rho(r) + \rho_{wat}(r) \quad (4)$$

$$z_{tot}(r) = \int_0^r 4\pi r'^2 \rho_{tot}(r')dr' \quad z(r) = \int_0^r 4\pi r'^2 \rho(r')dr' \quad (5)$$

$$E(r) = \frac{z_{tot}(r)}{r^2} D(r) = \frac{z(r)}{r^2} = E(r)\epsilon(r) \tag{6}$$

$$\phi(r) = \int_r^\infty E(r')dr' \tag{7}$$

where $\rho(r)$ is the charge distribution of NP plus counterions, while $\rho_{tot}(r)$ additionally includes the charge distribution of the solvent $\rho_{wat}(r)$. Equation 6 could be considered an alternative route (viii) to obtain $\epsilon(r)$ since $D(r)$ and $E(r)$ can be evaluated independently. $\epsilon(r)$ can be even directly evaluated from the polarization field of water from trajectories (route ix):

$$\rho_{wat}(r) = \delta^+ n_H(r) + \delta^- n_O(r) z_p(r) = \int_0^r 4\pi r'^2 \rho_{wat}(r')dr' \tag{8}$$

$$P(r) = -\frac{z_p(r)}{4\pi r^2} \epsilon(r) = 1 + \frac{4\pi P(r)}{E(r)} = \frac{1}{1 - 4\pi P(r)/D(r)} \tag{9}$$

where $\delta^+ = +0.41$ and $\delta^- = -0.82$ are the effective charges of H and O in water and $n_H(r)$ and $n_O(r)$ are their radial densities, respectively. In (eq 9), one can consistently use E (or D) from (eqs 4–6).

Debye–Hückel Screening. Mobile ions are treated implicitly in the Poisson–Boltzmann equation

$$-\nabla\epsilon(\mathbf{r})\nabla\phi(\mathbf{r}) = \rho_{NP}(\mathbf{r}) + \sum_i n_i q_i e^{-q_i\phi(\mathbf{r})/kT} \tag{10}$$

which assumes that the equilibrium distribution for ions with bulk density is n_i. At low concentrations, eq 10 can be linearized, leading to the Debye–Hückel (DH) potential[53]

$$\phi(r) = \frac{Z}{\epsilon_\infty(1 + \kappa R)} \frac{e^{-\kappa(r-R)}}{r} \quad r > R \tag{11}$$

$$\kappa = \frac{1}{\lambda_D} \lambda_D = \sqrt{\epsilon_\infty kT/4\pi e^2(n_+ + n_-)} \tag{12}$$

$$\Delta\rho_\pm(r) = z_\pm \Delta n_\pm(r)$$
$$= -n_\pm \frac{z_\pm^2 Z}{\epsilon_\infty kT(1 + \kappa R)} \frac{e^{-\kappa(r-R)}}{r} \Theta(R - r) \tag{13}$$

where R and Z are the radius and charge of the NP, respectively (further assumed to have an exactly neat spherical surface), $n_\pm$ is the density of positive and negative ions, and $\Delta\rho_\pm$ is the ion charge variation. In principle, formulas 11–13 depend only on parameters Z, $n_\pm$, and R, which could be evaluated based on the analysis of radial distributions. In practice, however, R can be defined in multiple ways and is ill-defined in the presence of anisotropy, and the evaluation of $n_\pm$ is difficult in small cells and in the presence of tightly bound counterions. To account for these effects, the renormalization of n, Z, and R has been previously proposed.[54] Considering that we can evaluate all of the charge–density components separately, we are in the position of using (eq 11) or (eq 13) to fit the values of those parameters on the potentials and ion charge densities evaluated from atomistic simulations (route x). This will finally result in ionic strength-dependent analytical potentials fitting the numerical ones and including charge and size renormalization effects.

RESULTS AND DISCUSSION

The following sections report the analysis of the simulations and the derivation of the structural and electrostatic properties.

Size and Shape of the NPs. Figure 2 reports the space distributions and $g(r)$ of a selected group of atoms (see the caption) of the ligands from the simulations at low ionic strength. The isosurfaces of spatial distributions reveal some degree of anisotropy, especially for the NP-Phe, reflecting the symmetry of the Au core that the small functional groups are not able to mask, and for the NP-COO, whose side chains are aligned to form protruding lobes. Conversely, in NP-NH3 and NP-Arg, the more disordered chain distribution results in a globular shape. In general, however, anisotropy and fluctuations rapidly decay with the distance from the surface already within 4−5 Å. Therefore, the structural radii (Table 2) turned

Table 2. Structurally and Electrostatically Defined Particle Radii[a]

	R_g (Å)	R_{av} (Å)	R_{max} (Å)	R_ϵ, σ (Å)
1	8.3	10.1	11.6	9.6, 1.0
2	14.2	18.0	20.8	15.4, 1.8
3	13.8	17.4	20.6	15.4, 1.9
4	13.8	17.6	20.4	15.4, 1.9
5	13.8	17.5	20.5	15.4, 1.9
6	19.2	26.1	32.7	19.1, 3.1
7	19.5	24.2	34.4	18.7, 3.8
8	18.8	21.3	33.1	18.7, 4.0
9	18.8	21.2	33.0	19.1, 3.6
10	18.2	20.9	30.8	19.1, 3.1
11	23.5	29.8	37.6	23.9, 3.2
12	20.8	23.8	36.0	22.7, 3.2
13	21.3	24.6	36.3	22.6, 3.1
14	20.9	23.4	35.5	22.8, 2.9
15	20.8	23.4	35.1	21.8, 3.6

[a]All quantities averaged over the production runs, i.e., the equilibrated parts of the trajectories. R_g, gyration radius; R_{av} and R_{max}, average and maximum values of the distance of the apical group from the NP center; R_ϵ, σ, switching parameters of the dielectric function.

out to be reasonably well-defined. R_{max} and R_{av} are larger than R_g and related to the external surface of the NP. Accordingly, the space distribution of the apical group (green isosurfaces in Figure 2) generally describes the external surface, and the maxima of the corresponding $g(r)$ are approximately located at R_{av}, which turns out to be a reasonable definition of the NP physical radius.

We observe a correlation between the R's (investigated more in-depth in the next sections): R_{max} is $\sim 1.5 \times R_g$. The effect of the ion screening is more visible in R_{max}, which is seen to decrease as the ionic strength increases as the NPs assume a more compact structure. The trend is in line with available experimental dynamic light scattering data for NP-COO and NP-ARG, reporting a reduction in the hydrodynamic radius at large ionic strength.[9] The behavior is, however, not linear, showing a "saturation" at high ionic strength to a limiting radius. Figure 3 shows that for NP-Arg (panels c,f), the contraction saturates at 100 mM, while for NP-COO (panels b,e), it is even more irregular and nonmonotonic, with the size at 50 mM smaller than at 100 mM, indicating a more complex internal organization of the chains. In our previous work,[14] this has been associated with the presence of Na$^+$ counterions in the vicinity of the carboxylic end groups, which, at variance
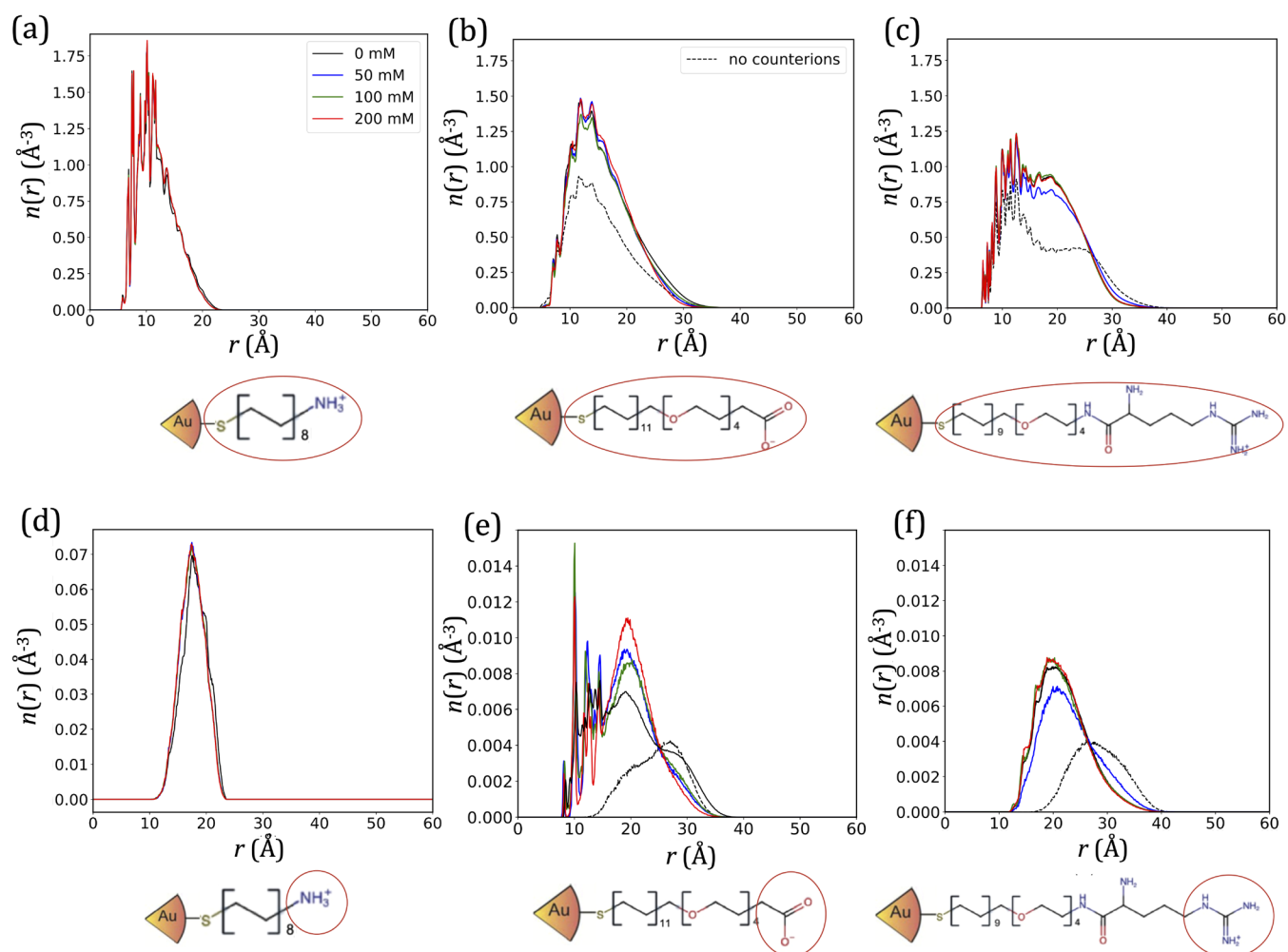
Figure 3. $n_{NP}(r)$ at different ionic strengths for NP-NH3 (a, d), NP-COO (b, e), and NP-Arg (c, f) for all NPs excluding Au (a, b, c) or only apical groups (d, e, f). The ionic strengths (excess values) are reported in the legends (only in first plots, same color/line coding, where not reported).

with the NP-Arg case, extend in elongated conformations at low ionic strengths. Accordingly, Figure 3e shows increased COO⁻ apical group density near the NP surface (10−12 Å) at large ionic strengths, appearing as a noisy shoulder (solid lines) not present in the absence of counterions (dashed black line), indicating inward bending of the chains, while in the NP-Arg (f), the effect seems less pronounced.

Charge Structure of NPs. The analysis of the charge structure of NPs at different ionic strengths is reported in Figure 4. The volume charge−density maps $\rho(\mathbf{r})$ of NP+ions at null excess ionic strength (i.e., with only neutralizing counterions) are reported under the plots as iso-density surfaces of different positive (red) and negative (blue) densities showing the charge shell alternation (in each case, iso-density values are chosen to select the three outer charge shells). The charge alternation structure is also visible in the radial charge densities $\rho(r)$ reported in the plots, either in those of the NPs alone (blue dotted line in panel a and top plots in panels b−d) or in the total NP+ions (green solid line in panel a and bottom plots of panels b−d). The $\rho(r)$ calculated with routes (i) and (ii) reveals only negligible differences (details in the SI); therefore, in the following, (i) is used when not otherwise specified.

Specifically, in NP-Phe, the first positive peak indicates the charge of the gold core, and the negative fluctuactions the

polarization of the sulfur head groups of the thiol ligands, located at ∼5 Å in this NP, being the Phe functional group almost overall neutral. The very low Na⁺ density extending only out of the NP (red line) in this case does not appreciably contribute to the NP or the total charge structure. The negative shell due to S is also visible in NP-NH3 $\rho_{NP}(r)$, located in this case at ∼9 Å (top plot of panel b), with the other relevant feature in this case being the positive peak at ∼17 Å due to NH3 apical groups. The charge profile shows little dependence on the ionic strength (lines in different colors are nearly superimposed). Indeed, Cl⁻ counterions (solid colored lines in the middle plot b) accumulate corresponding to the positive peak of $\rho_{NP}(r)$, confirming their association with the NH₃⁺ apical groups, and also show some amount of penetration down to the gold core. As the ionic strength increases, however, Cl⁻ distribution is seen to vary, especially across the R_{max} outward, where the DH tail accordingly increases. The positively charged Na⁺ ions appear to be distributed out of the particle ($>R_{max}$) namely at farther distances, and at increasing ionic strength their bulk density increases, as expected. The main influence of ionic strength on the total $\rho(r)$ is observable in the region between 10 and 25 Å, where the increasing density of Cl⁻ almost neutralizes the positive peak of the NH₃⁺ group.
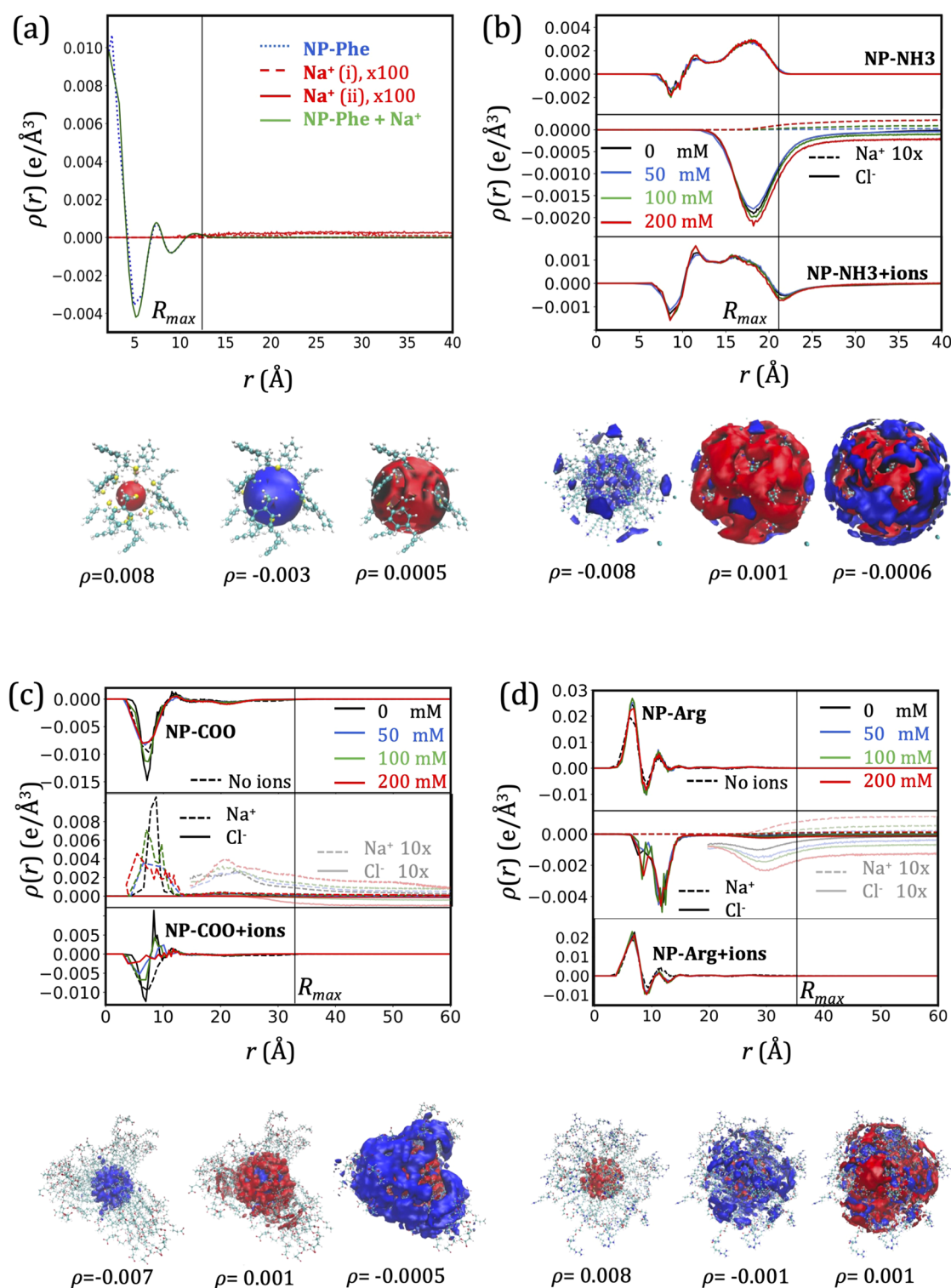
Figure 4. Radial and space distribution functions of the NPs and ion charges for NP-Phe (a), NP-NH3 (b), NP-COO (c), and NP-Arg (d). Subpanels in panels (b), (c), and (d) represent NP-only atoms (top), ions (middle), and total charge distributions (bottom). The color and line coding is reported in the legend (excess-only ionic strengths are reported for simplicity). Where indicated, ion densities are also shown expanded ($\times 10$). The total (NP + ions) $\rho(\mathbf{r})$ are also represented as isocharge surfaces in blue (negative) or red (positive, isovalues reported) for the null excess ionic strength case. Vertical lines indicate the R_{max}.

The charge shell organization in the large NPs (panels c and d) is more complex. In both cases, the $\rho_{NP}(r)$ (top plots) shows an alternating shell organization, which appears dominated by the negative charge of the S groups (at ~9 Å) and, in the case of NP-Arg, even by an inner positive shell, due

to the polarization of the outer layers of Au atoms. Smaller oscillations are visible up to the R_{max} distance due to chain polarization and charge of apical groups. In NP-COO, the structure is visibly more sensitive to ionic strength (different colored lines), especially near the core surface.
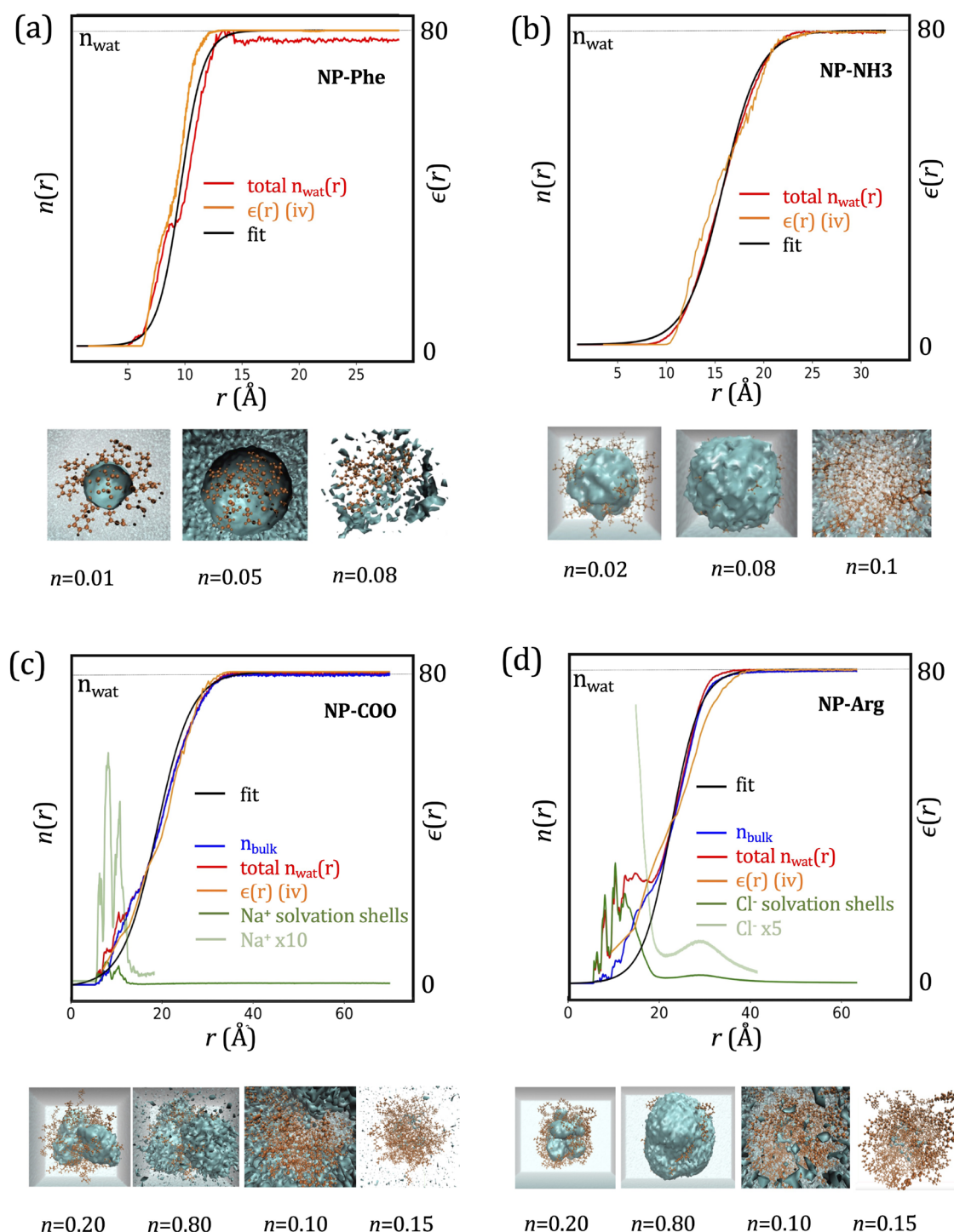
Figure 5. Volume and radial density of water (a) NP-Phe, (b) NP-NH3, (c) NP-COO, and (d) NP-Arg at null excess ionic strength (simulations no. 1, 2, 7, and 12). Color coding: red, total; green, water hydrating inner counterions (hydration shell = within 3 Å of the ion); blue, "bulk" water; black, fitting of the ϵ form bulk water in (c) and (d) and of the total in (a) and (b); and orange, dielectric function from SASA (iv). The bulk value density of water is reported (horizontal thin line labeled as n_{wat}). Under the plots, iso-density surfaces are reported in light blue (density isovalues indicated) superimposed on reference structures.

The ion distributions (middle plots of c and d) clearly show that counterions (Na$^+$ for NP-COO and Cl$^-$ for NP-Arg) accumulate well within R_{max} and near the gold core. In particular, in NP-Arg (d, solid lines in the middle plot), these "inner" counterions form two subshells at ∼10 and ∼12 Å, showing little dependence on ionic strength, while in the case of NP-COO, they form a disordered distribution, broadening as the ionic strength increases (dashed lines of different colors in panel c, middle plot). The apparently more ordered ion organization of NP-Arg is likely due to a different chain flexibility and the lower mobility and penetration capability of the larger Cl$^-$ (1.81 Å) with respect to smaller Na$^+$ (0.98 Å). In both cases, however, a second broader counterion shell is present, shown to be associated with the charged apical group
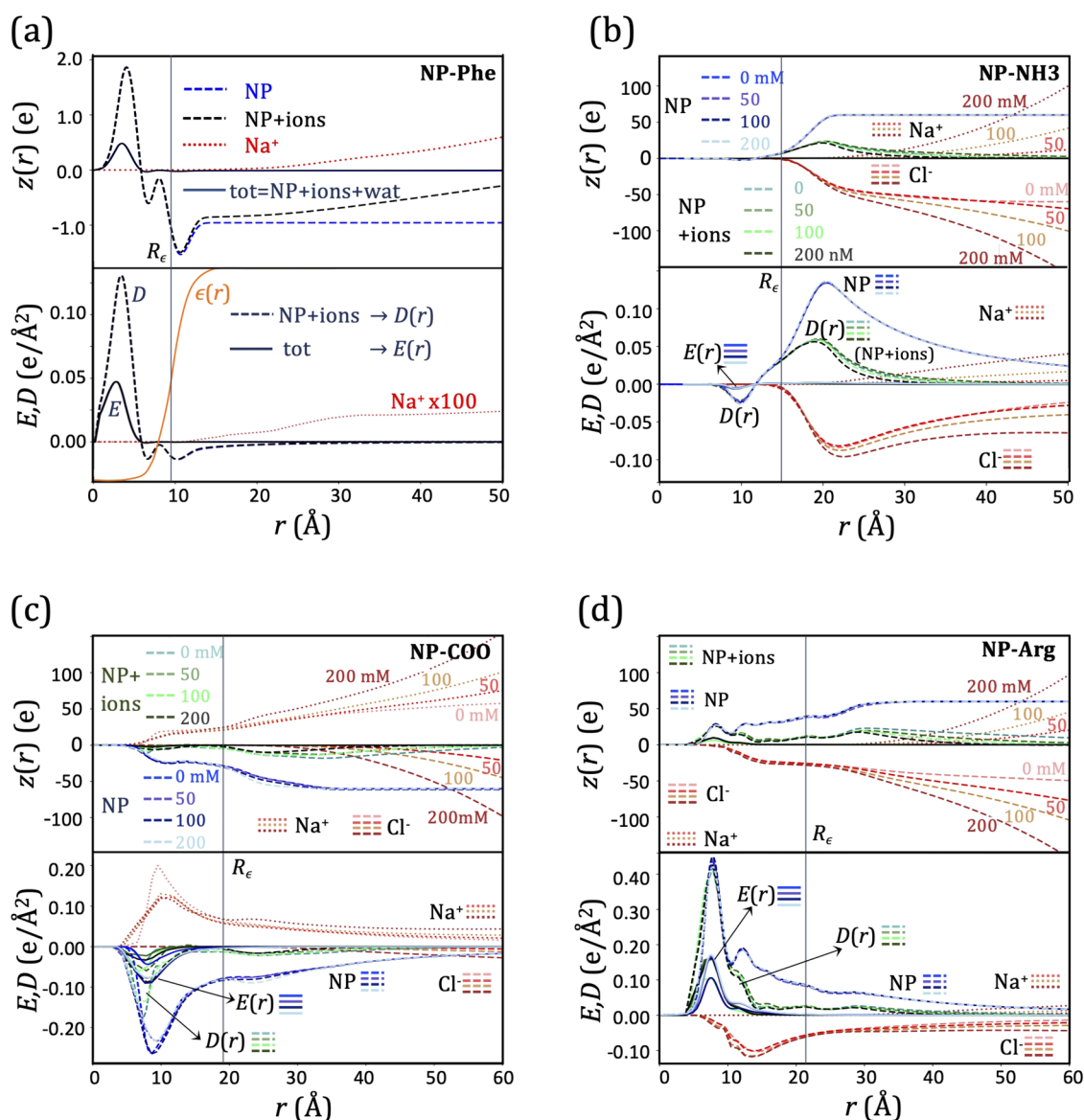
Figure 6. Integrated radial charge (upper plots) and fields (lower plots) for NP-Phe (a), NP-NH3 (b), NP-COO (c), and (d) NP-Arg, shown in separated components as per legends (route vii). In (b–d), calculations for different ionic strengths are reported in different shades as per legends. The value of R is reported as vertical lines. The fitted (r) is also reported in orange in (a).

by MD simulations,[14] better visible in the 10× expanded views (same colors and lines, but lighter shades in the middle plots of c and d). This is well-defined and located at ∼30 Å in NP-Arg, while it is broader and around ∼20−22 Å in NP-COO. These outer shells continuously connect with the DH tail across R_{max} and, at variance with the inner shells, increase visibly as the ionic strength increases. The same sign ions (better visible in expanded views) behave as expected, extending especially beyond R_{max} to increasing plateaus as the ionic strength increases.

The combination of ρ_{NP} with ρ_{ions} returns a rather different behavior of $\rho_{tot}(r)$ in the two NPs (bottom plots in parts c and d), especially when regarded as a function of ionic strength. In NP-Arg, the increasing ionic strength alters $\rho_{tot}(r)$ only superficially, leaving the internal Cl⁻ shells. Conversely, in NP-COO, the more mobile Na⁺ penetrates down to the core and neutralizes almost totally the internal charge polarization at 200 mM (red solid line in c, bottom plot). These differences are paralleled by a different behavior of the chain dynamics.[14]

As the ionic strength increases, NP-COO undergoes a "transition" from a three-lobe structure to a more compact globular one due to an internal reorganization of the counterions and a partial inward folding of the chain apexes, while some of them remain extended and fluctuating. These observations are coherent with the previously noted non-monotonic behavior of the NP radii as a function of the ionic strength.

Water Penetration and Dielectric Function. Figure 5 reports the radial and space distributions of water molecules and (r), evaluated for the four NPs (same simulations as in Figure 4). The red line is $n_{wat}(r)$, directly proportional to $\epsilon(r)$ (route ii + iii). The orange line is $\epsilon(r)$, evaluated by means of the volume maps of water accessibility $\rho_{wat}(\mathbf{r})$ and a subsequent spherical average (route iv). The two determinations are generally in qualitative agreement, especially for the small NPs, where the small discrepancies at the NP boundary can be attributed to the different definitions of water accessibility and averaging procedures. The data are used to

Table 3. Effective NP Charges and Debye Lengths: Z, Bare NP Charge; $\tilde{Z}$, Renormalized NP Charge by the Trapped Ions; and λ_D, Bare Debye Length[a]

	Z	$\tilde{Z}$	$\tilde{z} = \tilde{Z}/\epsilon_\infty$	λ_D (nm)	fit on ϕ			fit on $\Delta\rho_\pm$
					$\lambda_\phi^{(v)}$ (nm)	$\lambda_\phi^{(vi)}$ (nm)	$\lambda^{(vii)}$ (nm)	$\lambda_\rho^{(i)}$ (nm)
1	−1	−1	−0.013	6.92	2.3	1.8	1.9	*
2	+60	+55	+0.69	0.67	0.69	0.69	0.66	0.69
3	+60	+55	+0.69	1.10	1.12	1.13	1.11	1.11
4	+60	+55	+0.69	0.73	0.76	0.71	0.79	*
5	+60	+55	+0.69	0.50	0.48	0.52	0.53	*
6	−60	−60	−0.65	∞	*	*	1×10^2	*
7	−60	−37	−0.46	2.28	2.02	2.30	2.27	2.24
8	−60	−35	−0.44	1.20	1.25	1.22	1.21	1.20
9	−60	−34	−0.43	0.89	0.91	0.92	0.91	0.91
10	−60	−31	−0.39	0.66	0.77	0.79	0.66	*
11	+60	+60	+0.65	∞	*	*	2×10^5	*
12	+60	+33	+0.41	2.23	2.03	2.16	2.14	2.22
13	+60	+35	+0.44	1.20	1.16	1.22	1.22	1.22
14	+60	+33	+0.42	0.89	0.87	0.90	0.89	0.92
15	+60	+33	+0.42	0.66	0.67	0.63	0.65	0.66

[a]The other λ's are determined fitting either on the potential or on the ionic charge (as Indicated) and using the indicated calculation. * Indicates undetermined fit.

fit the function $\epsilon(r)$ with eq 1 (black line), and the fitting parameters R_ϵ and σ are reported in Table 2.

Larger NPs (c, d) display more complex profiles. The total $n_{wat}(r)$ evaluated from simulations (red line) reveals the presence of water even near the gold surface at ∼9 Å and to 15−20 Å. Considering the presence of counterions in that region, we evaluated the part of $n_{wat}(r)$ due to their hydration shells (green lines, also expanded view in lighter shades), which, in fact, reflects the distribution of counterions (see panels c and d in Figure 4). Once this is subtracted from $n_{wat}(r)$ to obtain $n_{bulk}(r)$ (blue lines), the profile is smoother and more similar to that obtained from route (iv) (orange line) and can be used for the fit of $\epsilon(r)$. On average, on all of the simulations (see Table 2), R_ϵ turns out slightly larger than R_g and ∼20% smaller than R_{max}. While R_ϵ is a measure of the average water penetration distance, R_{max} is rather the outer limit of the NP extension.

Figure 5 also reports the volume density maps of water, represented as isosurfaces, for different density isovalues. These confirm the more accentuated anisotropy for the larger NPs, especially NP-COO. For the smaller NPs, the larger water concentration is found in proximity to the surface, while for the larger NPs, the internal water penetration is visible, revealing the presence of the internal ion hydration shells. Further details are reported in SI, Section S.4.

Electrostatic Fields. Figure 6 reports the integrated radial charge $z(r)$ and the fields E and D evaluated from the $\rho(r)$s (route vii) for the different NPs, separated in components (NPs, ions, and water). The $z(r)$ plot of NP-Phe (Figure 6a, upper panel) confirms that counterions do not penetrate the NP (red line), which makes the NP and NP+ions charge (blue and black dashed lines) coincide up to the particle radius, while out of it, the NP charge is gradually screened by the counterions, as shown by the NP+ions charge (dashed black line). The effect of water is visible in the total $z(r)$ (black solid line): as expected, it is dramatically reduced out of the NP, while inside the effect is smaller. Accordingly, $\epsilon(r)$ (reported in the lower plot in orange) starts decreasing at 10 Å, reaching ∼1 at ∼5 Å. The ratio between the displacement D and electric E fields, obtained from the NP+ions and total charges,

respectively, follows $\epsilon(r)$, clearly showing the suppression of E out of the NP. Given the extremely low ionic strength, the contribution of counterions is very small (red dotted line, expanded ×100), generating no appreciable effect on the fields.

For NP-NH3 (panel b), we report the results for the four simulations at increasing ionic strengths. The top panel shows that the NP radial charge regularly increases to the total charge value (+60) and is basically independent of the ionic strength (dashed lines in blue shades). In this case, however, the ions' integrated charges (dotted and dashed lines of red shades for Na$^+$ and Cl$^-$, respectively) are large and contribute substantially. As previously observed, Na$^+$ increases only out of the R_{max}, while Cl$^-$ penetrates also within the chains toward the gold core. In a shell of about 4−5 Å out of R_ϵ, the $z(r)$ of Cl$^-$ increases, but independent of the ionic strength, indicating the presence of ∼5 counterions stably bound to the NP, having the effect of renormalizing the NP charge to a value of $\tilde{Z} = +55$ (see Table 3). Out of the NP, conversely, the Cl$^-$ contributes to a DH-like ion density-dependent screening shown in the NP+ions $z(r)$ (green lines of different shades) and is better visible comparing the NP-only and NP+ions fields (i.e., $D(r)$, green shaded lines) in the lower plot: the screening is stronger as the ionic strength increases, as expected. In this plot, we also reported $E(r)$s as solid lines (blue shaded), strongly suppressed out of R_ϵ, and only barely visible within it.

The behavior in the large NPs is homologous although more complex. The ions carrying the same charge of the NP (e.g. Cl$^-$ for NP-COO, panel c, and Na$^+$ for NP-Arg, panel d) show an increased bulk density in the NP outer region at increasing ionic strenght. As in NP-NH3, the $z(r)$ of the counterions (Na$^+$ for NP-COO and Cl$^-$ for NP-Arg) penetrates toward the core, displaying a plateau in the range of 10−20 Å, little sensitive to the ionic strength. In this case, the corresponding number of "trapped" counterions is 23−26 for NP-COO and 25−27 for NP-Arg, producing noticeably reduced $\tilde{Z}$ (see Table 3). The ionic strength-dependent screening is visible also in this case in ion charge for $r > 30$ Å. The fields (lower plots) behave accordingly and similarly to NP-NH3, except for the more variegated oscillation near the core. The $D(r)$ (blue and green dashed lines) starts separating for $r > 9−10$ Å, a distance
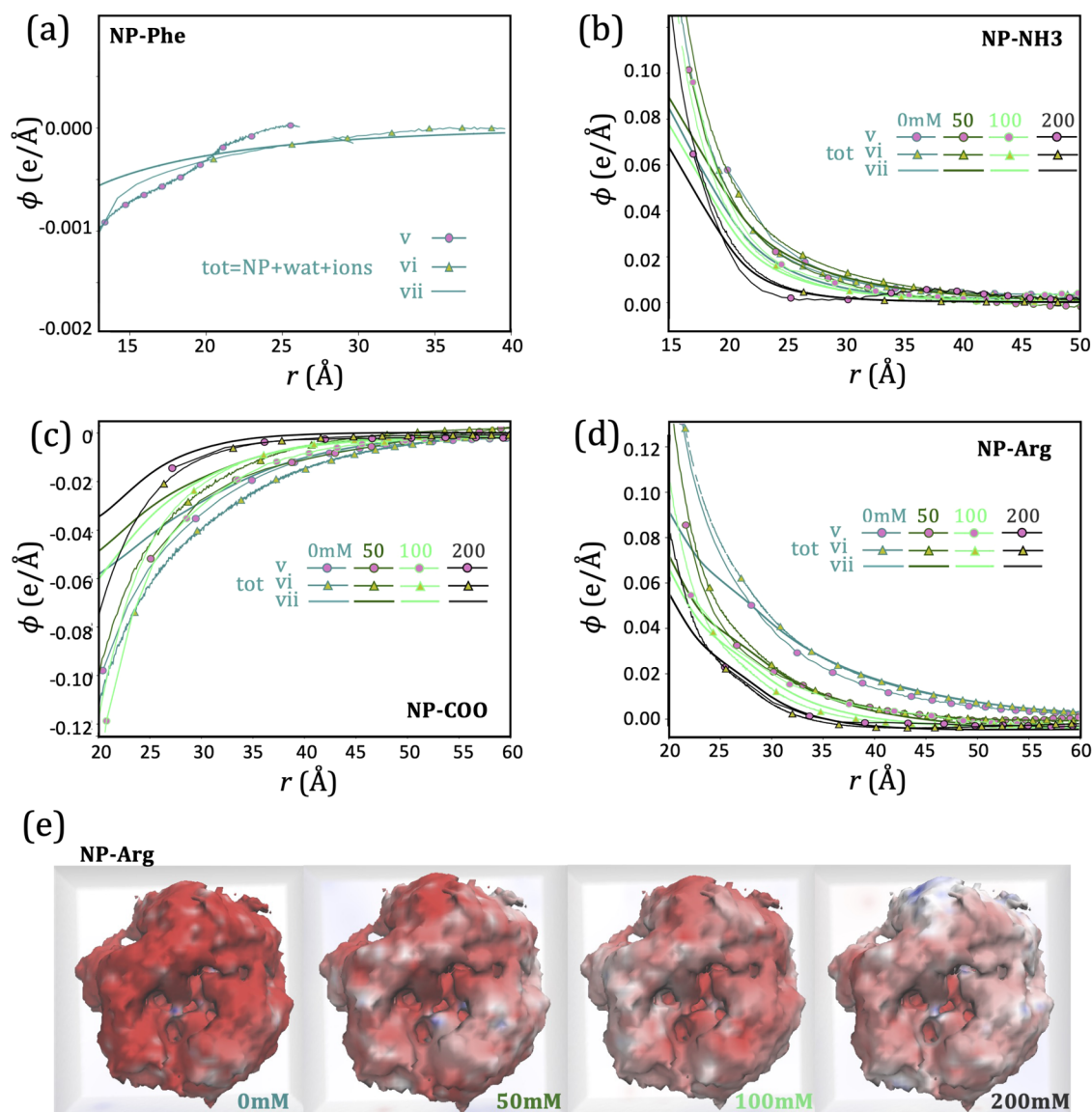
Figure 7. Total electrostatic potentials for (a) NP-Phe, (b) NP-NH3, (c) NP-COO, and (d) NP-Arg. Different ionic strengths are in different shades as per legends. Different symbols show the different calculations according to routes (v), (vi), and (vii). In panel (e), the $\phi(\mathbf{r})$ of NP-Arg at the reported ionic strength is mapped onto the solvent-accessible surface (isosurface of the water density map; see also Figure 5) colored according to the local ϕ: in red shades for positive values, white for null, and blue for negative (extremal values of the range ~0.05 e/Å).

at which the ions penetrate. As previously, the total field $E(r)$ is visible only in the region near the core, being strongly suppressed as $\epsilon(r)$ increases.

Potentials and Debye−Hückel Function Fitting. Following up on route vii, we evaluated all of the electrostatic potential components in all cases, reported in the Supporting Information (Section S.8). In Figure 7, we focus on their behavior for $r > R_e$, where the DH potential is fitted. The plots report the total $\phi(r)$ (i.e., NP + ions + water screening) at different ionic strengths. Calculations performed according to vii (plain lines) are compared to those from alternative routes v and vi (lines with symbols). In general, all of the methods are in good agreement for $r > R_{max}$, except in the case of NP-Phe, where the total ϕ evaluated with (v) shows a discrepancy from the others, while in all cases, the discrepancy is larger as R decreases to R_{max} and below. While in the former, we can attribute the discrepancy to the low statistics of counterions (it is not present in the NP-only ϕ; see the SI), short distance

discrepancy is more likely due to anisotropy, manifesting especially near the particle surface. In different methods, the radial averaging is performed at different levels of the procedure, which may give different weights to anisotropy, manifesting especially in the less globular NP-COO. Overall $\phi(r)$ at different ionic strengths (shades of green), although all vanishing at large r, display a faster decay as the ionic strength increases as expected, determining therefore noticeably different values of ϕ at the particle surface. This is a measurable quantity often referred to as the ζ-potential.

We investigate this aspect in more detail in the case of NP-Arg by mapping the value of ϕ onto the solvent-accessible surface (panel e). The SAS is evaluated as in Figure 5 as an isosurface of the $\rho_{wat}(\mathbf{r})$ (from simulation 12), and the local value of $\phi(\mathbf{r})$ from simulations 12−15 is reported on the surface in shades of red for positive values and of blue for negative values (see the color bar). Clearly, at low ionic strengths, the average value of the potential is higher (more
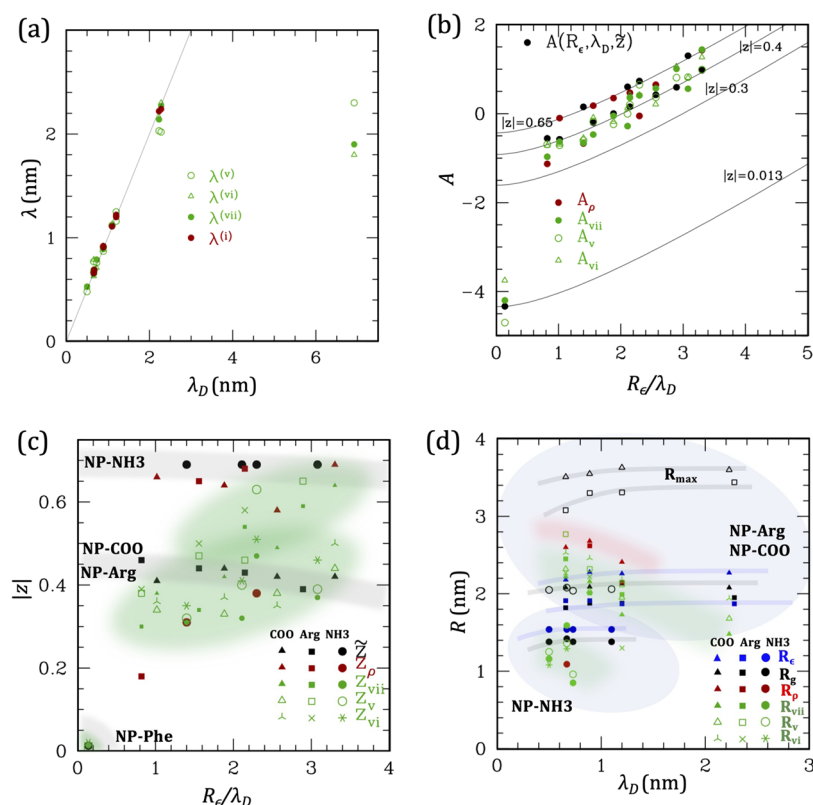
Figure 8. Parameters from DH fitting. (a) Debye lengths fitted on the determinations of $\phi(r)$ and ionic $z(r)$ compared to the λ_D from the bare ion density. Color coding has been reported in the legend; see Table 3 for labeling. Black line is for $\lambda = \lambda_D$. (b) Values of A fitted on the ion density and potentials (red and green, as per legend) and calculated from R_ϵ, λ_D, and $\tilde{z}$ (black dots), all plotted vs R_ϵ/λ_D. Constant z lines of the $A(R, \lambda, z)$ function are drawn in black with the z value reported. (c) Charges obtained from the fitting procedure with $R = R_\epsilon$ and $\lambda = \lambda_D$ (red and green) plotted as vs R_ϵ/λ_D compared to $\tilde{z}$ (black). Different symbols as per legend. Shaded areas are to guide the eye. (d) Radii obtained from the fitting procedure (in red and green, fixing $z = \tilde{z}$ and $\lambda = \lambda_D$), compared to the structural ones (black symbols) and to R_ϵ (blue symbols) as a function of λ_D. Symbols of fitted radii are as per legend. Lines are drawn to guide the eye in colors corresponding to the dots. Shaded light-blue oval areas generally enclose data from the indicated particles.

Table 4. Fit of A, R, and z[a]

| | | | | R = R_ϵ | | | $z = \tilde{z}$ | | | | R = R_ϵ | $z = \tilde{z}$ |
	$A_\phi^{(v)}$	$A_\phi^{(vi)}$	$A_\phi^{(vii)}$	$z^{(v)}$	$z^{(vi)}$	$z^{(vii)}$	$R^{(v)}$	$R^{(vi)}$	$R^{(vii)}$	$A_\rho^{(i)}$	$z^{(i)}$	$R^{(i)}$
1	−4.70	−3.75	−4.20	−0.008	−0.020	−0.013	*	2.72	1.20	*	*	*
2	+0.65	+0.42	+0.41	+0.63	+0.51	+0.47	1.59	1.36	1.29	−0.05	+0.38	1.09
3	−0.60	−0.55	−0.66	+0.32	+0.35	+0.31	*	*	*	−0.67	+0.31	*
4	−0.003	+0.13	−0.28	+0.40	+0.41	+0.32	0.85	0.96	*	*	*	*
5	+0.82	+0.81	+0.56	+0.39	+0.46	+0.37	1.16	1.25	1.08	*	*	*
6	*	*	−0.26	*	*	−0.77	*	*	*	*	*	*
7	−0.69	−0.72	−0.97	−0.38	−0.39	−0.30	*	*	*	−1.13	−0.18	*
8	−0.18	−0.09	−0.47	−0.47	−0.50	−0.34	1.99	2.12	1.30	+0.18	−0.65	2.15
9	+0.20	+0.42	+0.36	−0.46	−0.58	−0.54	2.01	2.32	2.22	+0.47	−0.68	2.62
10	+0.81	+1.06	+1.01	−0.65	−0.86	−0.59	2.45	2.77	2.27	*	*	*
11	*	*	−0.35	*	*	+0.70	*	*	*	*	*	*
12	−0.71	−0.69	−0.63	+0.34	+0.36	+0.38	1.48	1.68	1.94	−0.10	+0.66	*
13	−0.24	−0.18	−0.05	+0.33	+0.37	+0.42	1.73	1.95	2.18	0.35	+0.64	2.41
14	+0.37	+0.21	+0.57	+0.38	+0.35	+0.49	2.16	2.03	2.46	0.65	+0.58	2.68
15	+0.99	+1.27	+1.44	+0.44	+0.50	+0.64	2.22	2.32	2.53	+1.43	+0.69	2.60

[a]The first column reports the simulation numbering. Columns 2−3 report the fit of A_ϕ on the potential following methods (v)−(vii). Columns 5−7 and 8−10 have the charges or radii, respectively. Columns 11−13 report the fit of A_ρ on the ion density and the corresponding charges/radii. Radii are in nm, and charges are in e.

red) and decreases (going toward neutral, white) as the ionic strength increases. The value of the potential is variable due to anisotropy both of the surface and of the potential itself at these short distances, although anisotropy generally rapidly

decreases as the distance increases, except for the case of NP-COO (see the SI, Section S.8 for more details). The average value of ϕ on this surface is approximately the value of ϕ of

plot (d) at the average distance of the surface from the center, ~25 Å, and is related to the ζ-potential.

The total $\phi(r)$ (eq 11) and the ion density $\Delta\rho_\pm(r)$ (eq 13) can be used to fit the DH parameters in the ranges of exponential behaviors. These ranges are empirically identified in the bilogarithmic plots of $r\Delta\rho_\pm(r)$ or of $r\phi(r)$ as straight lines (SI, Section S.9, Figures S.10−S.12) and appear in all cases extending for 15−20 Å from R_{max}. In fact, depending on the particle radius, at smaller distances, the effects due to proximity of the NP chains appear, while beyond this limit, artifacts due to the finite cell size manifest. The values of $\kappa = 1/\lambda_D$ determined from the slope of the fitting lines are reported in Table 3 and plotted vs the bare λ_D value in Figure 8a. In general, the values λ_ϕ fitted on the different determinations of ϕ are in good agreement with each other, as expected, since in the fitting regions, the different ϕ's are basically superimposed (see Figure 7), and also with the values λ_ρ fitted on the ion densities, indicating the overall consistency of the different routes. Noticeably, all of them are also in good agreement with the λ_D from the bare ion density, especially $\lambda_\phi{}^{vii}$ and $\lambda_\rho{}^i$. The only exception is simulation 1, where the extremely low ion concentration implies λ_D comparable to the simulation cell size. This considered, we infer that the DH equation with the bare λ_D is a good approximation of at least up to 200 mM. In the following, we use $\lambda = \lambda_D$ to reduce the number of free parameters.

Conversely, the intercept of the fitting lines is a function of R/λ and $z = Z/\epsilon_\infty$

$$\ln(r\phi(r)) = -\frac{r}{\lambda} + A\ln\left(-\frac{rkT\rho(r)}{n_\pm z_\pm^2}\right) = -\frac{r}{\lambda} + A, \quad A$$
$$= \frac{R}{\lambda} + \ln\left(\frac{|z|}{1 + R/\lambda}\right) \quad (14)$$

where the first two equations are obtained from eqs 11 and 13, respectively. $\exp(A) = ze^{R/\lambda}/(1 + R/\lambda)$ is also the distance-independent prefactor of the DH potential. Therefore, the parameters R and z are not fittable separately but in the combination given by the function $A(R/\lambda, z)$, which can be inverted for the charge $|z| = (1 + R/\lambda)e^{A-R/\lambda}$. We then first fitted the parameters A_ϕ and A_ρ over (different determinations of) potential or ion densities. These are reported in Table 4, columns 2−4 and 11. Subsequently, to obtain radii or effective charges from $A_\rho(A_\phi)$, with $\lambda = \lambda_D$, we either let R = R_ϵ to obtain z or let $z = \tilde{z}$ to obtain R. This returns the new series of charges z^x associated with R (columns 5−7 and 12 of Table 4) or the new series of radii R^x associated with $\tilde{z}$ (columns 8−10 and 13 of Table 4) also plotted in Figure 8, panels (b−d).

Specifically, panel (b) reports the fitted values of A as a function of R_ϵ/λ_D (colored dots, color coding as in panel (a)) compared to those calculated using $\tilde{z}$ and R_ϵ, λ_D in eq 14 (black dots). Data are in generally good agreement with each other, although they are seen to spread among different constant z lines (reported in black from the analytic function $A(z, R_\epsilon/\lambda_D)$), indicating that z values, even for the same particles, are not exactly constant and equal to $\tilde{z}$. This is in fact more evident in panel (c), where the z values are reported as a function of R_ϵ/λ_D: $\tilde{z}$ (black symbols, shaded black lines) appears almost constant or weakly decreasing as the ionic strength increases. This is likely due to the fact that at higher ionic strengths the number of trapped counterions tends to increase. Conversely, the values of z obtained from the fit of A

letting R = R_ϵ (red and green symbols, green shaded areas) are very scattered but seem to show a different trend, rather weakly increasing with ionic strength.

The radii reported in panel (d) show a homologous behavior: the structural radii R_g, R_{max} (in black), and R_ϵ (in blue symbols) have already noted good correlations (see also the SI, Section S.10) and reveal an almost constant or slightly increasing trend as a function of λ_D (lines are shown to guide the eye). Conversely, the fitted radii obtained fixing $z = \tilde{z}$, $\lambda = \lambda_D$ (in colors as per legend) show a scattered behavior, though less than the fitted charges, revealing a rather opposite decreasing trend with λ_D (green and red shaded lines to guide the eye). On average, NP-NH3 and NP-Arg fitted radii tend to be smaller than the structural radii, while the NP-COO radius on average appears larger. The reason for these apparent discrepancies is that, as noted, the effective charges and radii cannot be fitted separately, but rather they combine in the value of A. On the other hand, the value of A, though quite scattered as well, reveals a clearer increasing behavior as a function of the ionic strength (panel (b)) in spite of the method of calculation. A fit of A as a function of the ionic strength is reported in the SI, and once this is used to close the relation among radii, charges, and λ, the trends of panels c and d emerge (see Section S.10).

◼ SUMMARY AND CONCLUSIONS

In this work, we have explored the structural and electrostatic properties of four gold NPs with different cores and different functionalizations, resulting in different global sizes, shapes, and charges, thoroughly analyzing data from atomistic molecular dynamics simulations performed at different ionic strengths.

The structural analysis reveals that the size, roughly described by the gyration radius R_g and by an external radius R_{max}, depends weakly on the ionic strength, except at the very low ones, where major anisotropy signatures are also present, especially for NP-COO. Interestingly, the structurally defined average radius R_g correlates fairly well with the radius defined by the water penetration R_ϵ, describing the switch distance of the dielectric function. This implies that R_ϵ can be considered a generic particle radius accounting for structural, electrostatic, and dielectric properties all together.

The charge distributions and their changes with ionic strength reflect the structural organization of the NP, the water penetration, and ionic distribution. A number of counterions are seen to stably bind to the NPs, especially the larger ones, where they penetrate through the chains to the gold surface, and their number is weakly dependent on the ionic strength. These must be considered as part of the NP itself, renormalizing the bare charge rather than contributing to DH screening. The number of counterions is evaluated for the different NPs and gives a first approximation of the renormalized charge value $\tilde{z}$.

The different components of radial charge, fields, and electrostatic potentials of the NP alone, ions, and water were evaluated separately. Anisotropies in the electrostatic potential are present in proximity to the surface, but they decay rapidly, except for the NP-COO. Overall, however, the radial representation of the potential and of the other electrostatic quantities allowed one to clearly identify the region where DH-like screening is observed. This turned out to start out of R_{max} and extend for 1.5−2 nm, enough to accurately fit the Debye length, which was found to be in good correlation with the one

calculated directly from the ion density, confirming that at these ionic strengths the DH picture is valid. In other words, while $R_c \sim R_g$ can be considered the average radius of the NP characterizing its "size", R_{max} can be considered the radius beyond which the NP can be safely described as a DH-like spherical object.

The other fittable parameter is the interaction strength A, which is a combination of R and z. Therefore, these cannot be fitted separately, and to obtain any of the two, the other must be given. When we did that, using different restrains on one of the two, the trend of the other as a function of the ionic strength turned out less clear and dependent on which restrain is imposed. This indicates that rather than R or z separately, the interaction strength A is the relevant quantity, which displays a regularly increasing behavior with ionic strength.

Overall, these findings allow schematizing the electrostatic behavior of these NPs at variable ionic strengths. To a good level of approximation, the NP-generated potential is obtained considering R_c as the NP radius, including a renormalized charge accounting for the screening due to trapped ions on the surface of the NP and further reduced as a function of the increasing ionic strength, which we evaluated quantitatively. However, the behavior as a function of the ionic strength is finely described by λ_D and A $(\tilde{z}, R_c, \lambda_D)$. These results can be used in simplified representations of the NPs for coarse-grained molecular dynamics simulations, possibly including shape effects by means of recently proposed advanced analytic representations of the potentials.[55,56]

In addition, we approximately evaluated the ζ-potentials as the values of ϕ on the SAS, whose average value is $\sim\exp(A(\tilde{z}, R_c, \lambda_D))$, showing its strong sensitivity to ionic strength. These results help interpret the literature data on electrostatic properties of metal NPs in saline solutions, which were extensively investigated. Colloidal stability is often associated with the ζ-potential, experimentally defined as the potential evaluated at the interface between the mobile ions and the dispersant. For high values of ζ, the solution or dispersion will resist aggregation, while if ζ is small, the dispersion may flocculate. We believe that our analysis and quantification of this parameter will help interpret the colloidal behavior.

In conclusion, our analysis will allow building coarse-grained and mesoscale models for the NPs accurately accounting for the electrostatics at different ionic strengths, based on the knowledge of a few parameters, and it shows the importance of combining bottom-up strategies with knowledge-based information to build models for *in silico* studies aimed at engineering nanoparticles with controlled interactions with biomolecules, for sensing, delivery, and imaging applications.

ASSOCIATED CONTENT

Ⓢ Supporting Information

The following files are available free of charge. The Supporting Information is available free of charge at https://pubs.acs.org/doi/10.1021/acs.jpcb.3c03481.

> NP structures; radial charge distributions; force fields and effective charge calculations; clustering of trajectories, solvent-accessible surfaces, and dielectric calculations; analytic solution of the dielectric sphere; radial distribution function and particle radii and their dependence on λ_D; and electrostatic potentials and Debye−Hückel fit (PDF)

AUTHOR INFORMATION

Corresponding Authors

Valentina Tozzini − *Institute Nanoscience-CNR, Lab NEST SNS, Pisa 56127, Italy;* ⓞ orcid.org/0000-0002-7586-5039; Email: valentina.tozzini@nano.cnr.it

Giorgia Brancolini − *Institute Nanoscience-CNR, Center S3, Modena 41125, Italy;* ⓞ orcid.org/0000-0002-1083-9198; Email: giorgia.brancolini@nano.cnr.it

Author

Margherita Bini − *Institute Nanoscience-CNR, Lab NEST SNS, Pisa 56127, Italy;* ⓞ orcid.org/0000-0002-7829-3507

Complete contact information is available at:
https://pubs.acs.org/10.1021/acs.jpcb.3c03481

Notes

The authors declare no competing financial interest.

ADDITIONAL NOTES

[a]For Au$_{144}$, where the center is void, a fictitious atom located at the center of the inner shell is added to the trajectory to be used in the calculation.

[b]APBS is normally used for the Poisson−Boltzmann equation (PBE) solution, but it can be used for PE by letting the implicit counterion concentration go to 0 and including it explicitly within $\rho(\mathbf{r})$.

REFERENCES

(1) Häkkinen, H. The gold-sulfur interface at the nanoscale. *Nat. Chem.* **2012**, *4*, 443−455.

(2) Alex, S.; Tiwari, A. Functionalized Gold Nanoparticles: Synthesis, Properties and Applications—A Review. *J. Nanosci. Nanotechnol.* **2015**, *15*, 1869−1894.

(3) Vlamidis, Y.; Voliani, V. Bringing Again Noble Metal Nanoparticles to the Forefront of Cancer Therapy. *Front. Bioeng. Biotechnol.* **2018**, *6*, 143−148.

(4) Chen, L. Y.; Wang, C. W.; Yuan, Z.; Chang, H. T. Fluorescent gold nanoclusters: recent advances in sensing and imaging. *Anal. Chem.* **2015**, *87*, 216−229.

(5) Klębowski, B.; Depciuch, J.; Parlińska-Wojtan, M.; Baran, J. Applications of Noble Metal-Based Nanoparticles in Medicine. *Int. J. Mol. Sci.* **2018**, *19*, 4031.

(6) Pelaz, B.; Alexiou, C.; Alvarez-Puebla, R. A.; et al. Diverse Applications of Nanomedicine. *ACS Nano* **2017**, *11*, 2313−2381.

(7) Marcinko, T. M.; Dong, J.; LeBlanc, R.; Daborowski, K. W.; Vachet, R. W. Small Molecule mediated Inhibition of β-2-Micro-

globulin Amyloid Fibril Formation. *J. Biol. Chem.* **2017**, *292*, 10630−10638.

(8) Miranda, O. R.; Creran, R.; Rotello, V. M. Array-based sensing with nanoparticles: 'Chemical noses' for sensing biomolecules and cell surfaces. *Curr. Opin Chem. Biol.* **2010**, *14*, 728−736.

(9) Ray, M.; Brancolini, G.; Luther, D. C.; Jiang, Z.; Cao-Milan, R.; Cuadros, A. M.; Burden, A.; Clark, V.; Rana, S.; Mout, R.; Landis, R.; Corni, S.; Rotello, V. Biomolecules gold-surface interaction: an optimized force field. *Nanoscale* **2022**, *14*, 2411−2418.

(10) Charchar, P.; Christofferson, A. H.; Todorova, N.; Yarovsky, I. Gold Nanoparticles: Understanding and Designing the Gold-Bio Interface: Insights from Simulations. *Small* **2016**, *12*, 2394.

(11) Heikkilä, E.; Gurtovenko, A. A.; HMartinez-Seara; Häkkinen, H.; Vattulainen, I.; Akola, J. Atomistic Simulations of Functional Au144(SR)60 Gold Nanoparticles in Aqueous Environment. *J. Phys. Chem. C* **2012**, *116*, 9805−9815.

(12) Van Lehn, R. C.; Alexander-Katz, A. Structure of Mixed-Monolayer-Protected Nanoparticles in Aqueous Salt Solution from Atomistic Molecular Dynamics Simulations. *J. Phys. Chem. C* **2013**, *117*, 20104−20115.

(13) Xiong, Y.; Liu, X.; Xiong, H. Aggregation modeling of the influence of pH on the aggregation of variably charged nanoparticles. *Sci. Rep.* **2021**, *11*, No. 17386.

(14) Brancolini, G.; Rotello, V. M.; Corni, S. Role of Ionic Strength in the Formation of Stable Supramolecular Nanoparticle−Protein Conjugates for Biosensing. *Int. J. Mol. Sci.* **2022**, *23*, 2368−2386.

(15) Huang, R.; Luther, D. C.; Zhang, X.; Gupta, A.; Tufts, S. A.; Rotello, V. M. Engineering the Interface between Inorganic Nanoparticles and Biological Systems through Ligand Design. *Nanomaterials* **2021**, *11*, 1001.

(16) Kyrychenko, A.; Blazhynska, M. M.; Kalugin, O. N. Protonation-dependent adsorption of polyarginine onto silver nano-particles. *J. Appl. Phys.* **2020**, *127*, No. 075502.

(17) Chew, A. K.; Pedersen, J. A.; Lehn, R. C. V. Predicting the Physicochemical Properties and Biological Activities of Monolayer-Protected Gold Nanoparticles Using Simulation-Derived Descriptors. *ACS Nano* **2022**, *16*, 6282−6292.

(18) Monti, S.; Barcaro, G.; Sementa, L.; Carravetta, V.; Agren, H. Dynamics and self-assembly of bio-functionalized gold nanoparticles in solution: Reactive molecular dynamics simulations. *Nano Res.* **2018**, *11*, 1757−1767.

(19) Franco-Ulloa, S.; Riccardi, L.; Rimembrana, F.; Grottin, E.; Pini, M.; Vivo, M. D. NanoModeler CG: A Tool for Modeling and Engineering Functional Nanoparticles at a Coarse-Grained Resolution. *J. Chem. Theory Comput.* **2023**, *19*, 1582−1591.

(20) Gautham, S. M. B.; Patra, T. K. Deep learning potential of mean force between polymer grafted nanoparticles. *Soft Matter* **2022**, *18*, 7909−7916.

(21) Radic, S.; Davis, T. P.; Ke, P. C.; Ding, F. Contrasting effects of nanoparticle-protein attractionon amyloid aggregation. *RCS Adv.* **2015**, *5*, 105489−105498.

(22) Tavanti, F.; Pedone, A.; Menziani, M. C. Competitive Binding of Proteins to Gold Nanoparticles Disclosed by Molecular Dynamics Simulations. *J. Phys. Chem. C* **2015**, *119*, 22172−22180.

(23) Di Fenza, A.; Rocchia, W.; Tozzini, V. Complexes of HIV-1 integrase with HAT proteins: Multiscale models, dynamics, and hypotheses on allosteric sites of inhibition. *Proteins* **2009**, *76*, 946−958.

(24) Trovato, F.; Nifosì, R.; Fenza, A. D.; Tozzini, V. A minimalist model of protein diffusion and interactions: the green fluorescent protein within the cytoplasm. *Macromolecules* **2013**, *46*, 8311−8322.

(25) Vácha, R.; Linse, S.; Lund, M. Surface Effects on Aggregation Kinetics of Amyloidogenic Peptides. *J. Am. Chem. Soc.* **2014**, *136*, 11776−11782.

(26) Trovato, F.; Tozzini, V. Diffusion within the cytoplasm: a mesoscale model of interacting macromolecules. *Biophys. J.* **2014**, *107*, 2579−2591.

(27) Lopez, H.; Lobaskin, V. Coarse-grained model of adsorption of blood plasma proteins onto nanoparticles. *J. Chem. Phys.* **2015**, *143*, 243138−243150.

(28) Brancolini, G.; Tozzini, V. Multi-scale modeling of Proteins interaction with Functionalized Nanoparticles. *Curr. Opin. Colloid Interface Sci.* **2019**, *41*, 66−73.

(29) Bini, M. Low Resolution Models for Bio-functionalized Metal Nanoparticles. Master Thesis, Department of Physics, University of Pisa, 2021.

(30) Brancolini, G.; Lopez, H.; Corni, S.; Tozzini, V. Low-resolution models for the interaction dynamics of coated gold nanoparticles with β2-microglobulin. *Int. J. Mol. Sci.* **2019**, *20*, 3866−3881.

(31) Mereghetti, P.; Maccari, G.; Spampinato, G.; Tozzini, V. Optimization of Analytical Potentials for Coarse-Grained Biopolymers Models. *J. Phys. Chem. B* **2016**, *120*, 8571−8579.

(32) Leonarski, F.; Trovato, F.; Tozzini, V.; Les, A.; Trylska, J. Evolutionary algorithm in the optimization of a coarse-grained force field. *J. Chem. Theory Comput.* **2013**, *9*, 4874−4889.

(33) Bauer, G.; Gribova, N.; Lange, A.; Holm, C.; Gross, J. Three-body effects in triplets of capped gold nanocrystals. *Mol. Phys.* **2017**, *115*, 1031−1040.

(34) Pohjolainen, E.; Chen, X.; Malola, S.; Groenhof, G.; Häkkinen, H. A Unified AMBER-Compatible Molecular Mechanics Force Field for Thiolate-Protected Gold Nanoclusters. *J. Chem. Theory Comput.* **2016**, *12*, 1342−1350.

(35) Dutta, S.; Corni, S.; Brancolini, G. Molecular Dynamics Simulations of a Catalytic Multivalent Peptide−Nanoparticle Complex. *Int. J. Mol. Sci.* **2021**, *22*, 3624−3641.

(36) Abraham, M. J.; Murtola, T.; Schulz, R.; Páll, S.; Smith, J. C.; Hess, B.; Lindahl, E. GROMACS: High performance molecular simulations through multi-level parallelism from laptops to super-computers. SoftwareX. *Int. J. Mol. Sci.* **2015**, *1−2*, 19−25.

(37) Iori, F.; Di Felice, R.; Molinari, E.; Corni, S. GolP: An atomistic force-field to describe the interaction of proteins with Au(111) surfaces in water. *J. Comput. Chem.* **2009**, *30*, 1465−1476.

(38) Brancolini, G.; Toroz, D.; Corni, S. Can small hydrophobic gold nanoparticles inhibit 2-microglobulin fibrillation? *Nanoscale* **2014**, *6*, 7903−7911.

(39) Bayly, C. I.; Cieplak, P.; Cornell, W.; Kollman, P. A. A well-behaved electrostatic potential based method using charge restraints for deriving atomic charges: the RESP model. *J. Phys. Chem. A* **1993**, *97*, 10269−10280.

(40) Vanquelef, E.; Simon, S.; Marquant, G.; Garcia, E.; Klimerak, G.; Delepine, J. C.; Cieplak, P.; Dupradeau, F.-Y. R.E.D. Server: a web service for deriving RESP and ESP charges and building force field libraries for new molecules and molecular fragments. *Nucleic Acid Res.* **2011**, *39*, W511−W517.

(41) Hess, B.; Bekker, H.; Berendsen, H.; Fraaije, J. LINCS: A Linear Constraint Solver for Molecular Simulations. *J. Comput. Chem.* **1988**, *18*, 1463−1472.

(42) Bussi, G.; Donadio, D.; Parrinello, M. Canonical sampling through velocity rescaling. *J. Chem. Phys.* **2007**, *126*, No. 014101.

(43) Parrinello, M.; Rahman, A. Polymorphic Transitions in Single-Crystals—A New Molecular-Dynamics Method. *J. Appl. Phys.* **1981**, *52*, 7182−7190.

(44) Essmann, U.; Perera, L.; Berkowitz, M.; Darden, T.; Lee, H.; Pedersen, L. A smooth particle mesh Ewald method. *J. Chem. Phys.* **1995**, *103*, 8577−8593.

(45) Van Der Spoel, D.; Lindahl, E.; Hess, B.; Groenhof, G.; Mark, A. E.; Berendsen, H. J. C. GROMACS: Fast, flexible, and free. *J. Comput. Chem.* **2005**, *26*, 1701−1718.

(46) Humphrey, W.; Dalke, A.; Schulten, K. VMD: Visual molecular dynamics. *J. Mol. Graphics* **1996**, *14*, 33−38.

(47) Bini, M. Script for Spherically Averaging Spatial Distributions. GitHub repository, 2023, Section: Radial average spatial distributions, Average radial charge [Source code], 2023, https://github.com/MargheritaBini/Radial_average_spatial_distributions.

(48) Blossey, R.; Podgornik, R. Continuum theories of structured dielectrics. *Europhys. Lett.* **2022**, *139*, 27002.

(49) Voges, D.; Karshikoff, A. Continuum theories of structured dielectrics. *J. Chem. Phys.* **1998**, *108*, 2219.

(50) Li, L.; Li, C.; Zhang, Z.; Alexov, E. On the Dielectric "Constant" of Proteins: Smooth Dielectric Function for Macromolecular Modeling and Its Implementation in DelPhi. *J. Chem. Theory Comput.* **2013**, *9*, 2126.

(51) Baker, N. A.; Sept, D.; Joseph, S.; Holst, M. J.; McCammon, J. Electrostatics of nanosystems: application to microtubules and the ribosome. *Proc. Natl. Acad. Sci. U.S.A.* **2001**, *98*, 10037−10041.

(52) Hardy, D. J.; Wu, Z.; Phillips, J. C.; Stone, J. E.; Skeel, R. D.; Schulten, K. Multilevel Summation Method for Electrostatic Force Evaluation. *J. Chem. Theory Comput.* **2015**, *11*, 766−779.

(53) Denton, B. L.; Denton, A. R. Charge Renormalization, Thermodynamics, and Structure of Deionized Colloidal Suspensions. *Commun. Comput. Phys.* **2010**, *7*, 235−249.

(54) Denton, A. R. Poisson−Boltzmann theory of charged colloids: limits of the cell model for salty suspensions. *J. Phys.: Condens. Matter* **2010**, *22*, No. 364108.

(55) Derbenev, I. N.; Filippov, A. V.; Stace, A. J.; Besley, E. Electrostatic interactions between spheroidal dielectric particles. *J. Chem. Phys.* **2020**, *152*, No. 024121.

(56) Siryk, S. V.; Rocchia, W. Arbitrary-Shape Dielectric Particles Interacting in the Linearized PoissonBoltzmann Framework: An Analytical Treatment. *J. Phys. B* **2022**, *126*, 10400−10426.